

Valley filtering and valley-polarized collective modes in bulk graphene monolayers

Jian-Long Zheng(郑建龙) and Feng Zhai(翟峰)
Citation: Chin. Phys. B, 2024, 33 (**1**): 017203. DOI: 10.1088/1674-1056/acfd17
Journal homepage: http://cpb.iphy.ac.cn; http://iopscience.iop.org/cpb

What follows is a list of articles you may be interested in

Valley polarization in transition metal dichalcogenide layered semiconductors: Generation, relaxation, manipulation and transport

Hui Ma(马惠), Yaojie Zhu(朱耀杰), Yulun Liu(刘宇伦), Ruixue Bai(白瑞雪), Xilin Zhang(张喜林), Yanbo Ren(任琰博), and Chongyun Jiang(蒋崇云)
Chin. Phys. B, 2023, 32 (**10**): 107201. DOI: 10.1088/1674-1056/ace160

Emergence of correlations in twisted monolayer-trilayer graphene heterostructures

Zhang Zhou(周璋), Kenji Watanabe, Takashi Taniguchi, Xiao Lin(林晓), Jinhai Mao(毛金海), and Hong-Jun Gao(高鸿钧)
Chin. Phys. B, 2023, 32 (**9**): 097203. DOI: 10.1088/1674-1056/ace3a8

Controlled crossover of electron transport in graphene nanoconstriction: From Coulomb blockade to electron interference

Wei Yu(余炜), Xiao Guo(郭潇), Yuwen Cai(蔡煜文), Xiaotian Yu(俞晓天), and Wenjie Liang(梁文杰)
Chin. Phys. B, 2023, 32 (**7**): 077202. DOI: 10.1088/1674-1056/accf67

Tunable correlation in twisted monolayer-trilayer graphene

Dongdong Ding(丁冬冬), Ruirui Niu(牛锐锐), Xiangyan Han(韩香岩), Zhuangzhuang Qu(曲壮壮), Zhiyu Wang(王知雨), Zhuoxian Li(李卓贤), Qianling Liu(刘倩伶), Chunrui Han(韩春蕊), and Jianming Lu(路建明)
Chin. Phys. B, 2023, 32 (**6**): 067204. DOI: 10.1088/1674-1056/acc8c3

Spin and valley filter in strain engineered silicene

Wang Sa-Ke (汪萨克), Wang Jun (汪军)
Chin. Phys. B, 2015, 24 (**3**): 037202. DOI: 10.1088/1674-1056/24/3/037202

TOPICAL REVIEW — Valleytronics

Valley filtering and valley-polarized collective modes in bulk graphene monolayers

Jian-Long Zheng(郑建龙)[1] and Feng Zhai(翟峰)[1,2,†]

[1] *Department of Physics, Zhejiang Normal University, Jinhua* 321004, *China*
[2] *Zhejiang Institute of Photoelectronics, Zhejiang Normal University, Jinhua* 321004, *China*

(Received 4 June 2023; revised manuscript received 21 September 2023; accepted manuscript online 26 September 2023)

The presence of two sublattices in hexagonal graphene brings two energetically degenerate extremes in the conduction and valence bands, which are identified by the valley quantum number. Recently, this valley degree of freedom has been suggested to encode and process information, which develops a new carbon-based electronics named graphene valleytronics. In this topical review, we present and discuss valley-related transport properties in bulk graphene monolayers, which are due to strain-induced pseudomagnetic fields and associated vector potential, sublattice-stagger potential, and the valley-Zeeman effect. These valley-related interactions can be utilized to obtain valley filtering, valley spatial separation, valley-resolved guiding modes, and valley-polarized collective modes such as edge or surface plasmons. The present challenges and the perspectives on graphene valleytronics are also provided in this review.

Keywords: valleytronics, graphene, strain, valley-Zeeman effect, plasmons

PACS: 72.80.Vp, 73.20.Mf, 73.43.Cd, 85.35.–p **DOI:** 10.1088/1674-1056/acfd17

1. Introduction

In many crystal semiconductors, there exist several energetically degenerate minimums in the conduction band or maximums in the valence band. These nonequivalent extremes with the same energy, identified by a novel quantum number dubbed valley, are called valley points. As a counterpart of the spin degree of freedom (DOF), the valley DOF was suggested as a potential information carrier.[1–7] For this valleytronics routine to next-generation electronic devices, a fundamental step is to create a distinguishable valley population such as valley spatial separation and valley-polarized current. Valleytronic materials usually possess two or more valley points with large separation in momentum space. This feature is useful for circumventing inter-valley scattering due to thermal fluctuations, but is disadvantageous for manipulating valley states. Although the investigations on the valley DOF can be dated back to the 1970s,[1,2] valleytronics booms after the emergence of two-dimensional (2D) materials with honeycomb structures.

In hexagonal 2D materials such as graphene and monolayer transition metal dichalcogenides (TMDs), the presence of two nonequivalent sublattices leads to two valley points[8,9] (K and K') at vertices of the Brillouin zone. The carrier population in the specific K or K' valley behaves like a spin-up or spin-down state in a spin $1/2$ system. The manipulation of valley states in graphene is appealing due to the excellent transport properties of graphene. Valley-polarized current can be obtained from an unpolarized stream passing through a valley filter. The seminal proposal of graphene valley filter[10] requires a nanoribbon with zigzag edges and a sub-10 nm constriction. Valley spatial separation was predicted in a graphene n–p–n junction which relies on trigonal warping of the energy bands.[11] The valley-dependent beams were observed in a photonic graphene.[12] For an electron beam with a large incident angle traversing a grain boundary (named line defect) in polycrystalline graphene, nearly perfect valley polarization was predicted.[7,13] Valley-polarized local states were generated by an individual atomic-scale defect[6] such as single-carbon vacancy, nitrogen-atom dopant, and hydrogen-atom chemisorption.

Beyond the methods based on the precise control of nanostructures, the combination of intrinsic band properties with optics, mechanics, electrostatics, and nanomagnets can yield valley-contrasting current. It was predicted that intense light with proper time dependence can effectively break the inversion symmetry of graphene and distinguish the valleys.[14,15] Pure valley currents in gapped bilayer graphene were generated by femtosecond laser light combining optical frequency circularly polarized pulse and a terahertz frequency linearly polarized pulse.[16] Non-dissipative pure valley currents, akin to pure spin currents, offer the possibility to build electronic devices with low power dissipation. In a bulk graphene sheet, the combination of local magnetic fields and substrate strain can generate a remarkable valley polarization with gate-tunable polarity.[17–19] For strained graphene flakes under a uniform pseudomagnetic field[20] and

†Corresponding author. E-mail: fzhai@zjnu.cn

© 2024 Chinese Physical Society and IOP Publishing Ltd

real magnetic field, the two valley states are separated in space and energy, leading to a robust bulk valley polarization.[21] For a graphene p–n junction subject to a Gaussian-shaped strain and vertical magnetic field, an oscillating Hall conductance and valley-resolved Fano resonances showed up.[22] Valley polarization, valley inversion,[23] and valley-contrasting spatial confinement[24] of massless Dirac fermions were demonstrated experimentally in strained graphene under inhomogeneous pseudomagnetic fields and tunable real magnetic fields. Several physical effects were examined on strained graphene without external magnetic fields, such as valley electron optics,[25] valley-related guiding mode,[26] pure bulk valley current due to quantum pump[27,28] or light irradiation,[29] valley-polarized edge plasmons,[30–32] valley-Hall effect and nonlocal transport,[20,33,34] pseudomagnetic-field-induced Lorentz force, Aharonov–Bohm phase,[35] and focusing.[36] By placing metagate with specific geometries and bias voltages within a few nanometers on graphene, complete propagation band gaps were predicted for graphene surface plasmons with nontrivial valley-linked topological properties.[37] Due to suppressed intervalley scattering, one can further obtain highly-localized guiding plasmons without any reflections. Electrons in valleytronic materials with short-range potential scattering generally experience a valley contrasted intervalley-backscattering due to distinct momentum transfers. As a result, sizable valley pump effects can be obtained by passing charge current through a region of nonmagnetic disorder, as demonstrated numerically in Ref. [38]. For graphene electrons normally incident at a superlattice barrier, fully valley-selective Klein tunneling[39] was predicted when intervalley backscattering and valley contrast in pseudospin chirality are accounted for. The angle-averaged transmission can have a net valley polarization exceeding 75% for a 20-period barrier. For an n–n$^-$–n junction based on 2D graphene, valley filter and valley source functions were demonstrated theoretically[40] at small and large band-offset between the n and n$^-$-regions, which are enabled respectively by intra- and inter-valley scatterings and depend on the junction orientation.

In gapped graphene with broken inversion symmetry, the presence of valley-dependent intrinsic magnetic moment and Berry curvature were proposed to generate and detect valley polarization by magnetic and electric means.[41] In gapped graphene systems, topological kink states[42–44] were predicted to form on a domain wall of the gap term. Kink states in K and K' valleys possess opposite propagating velocities. These valley–momentum locking kink states were confirmed by transport measurements.[45,46] For a four-kink router device based on bilayer graphene, Li *et al.* demonstrated experimentally[47] the operations of a valley valve and a tunable electron beam splitter. Various applications of topological kink states were reviewed in Ref. [48]. In a two-terminal graphene system with a Dirac gap, it was shown theoretically that[49] valley-polarized output current can be achieved under the modulation of a single nanomagnet. A double-barrier structure consisting of electric and vector potentials can filter massive Dirac electrons based on their valley index.[50,51] For graphene subject to a combination of a magnetic and electric barrier, the Fermi velocity modulation on valley transport was reported theoretically.[52] In strained and gapped graphene, spin–valley spatial separation and valley-resolved surface magnetoplasmons were demonstrated theoretically.[53,54] The time-dependent lattice vibration of optical phonon modes was proposed to realize a topological valley pump in graphene.[55] Spin–orbit coupling and staggered potential in graphene could be generated by the proximity of a TMD monolayer,[56,57] which allows quantum spin Hall and valley Hall effects, giant spin lifetime anisotropy mediated by spin–valley locking,[58] and field-effect spin–valley locking.[59] For graphene under the proximity of some magnetic substrates, several interesting properties were discussed, including universal valley Hall conductivity,[60] valley-contrasting quantum anomalous Hall effect,[61] and valley filtering.[62] For graphene modulated by patterned dielectric superlattices,[63] Dirac gap was found by using an unfolding procedure, which leads to a robust transverse valley current against irregularities in the patterned dielectric.[64] In graphene-based devices with spatially varying regions of staggered potential, Aktor *et al.* reported[65] the emergence of valley-polarized bulk currents and nonlocal resistance fingerprints, which are robust against disorder.

In this topical review, we generally introduce the valley filtering effect and valley-polarized collective modes in bulk graphene monolayers, mainly based on our own works. For valleytronics in TMDs, readers can refer to recent reviews.[4,5] In Section 2, we present a general formulation of valley filtering in bulk graphene monolayers based on strain and staggered potential. In Section 3, the results of valley filtering and valley electron optics in strained graphene are summarized. In Section 4, we exhibit valley filtering in gapped graphene. In Section 5, we introduce valley-polarized collective modes in graphene, including edge plasmons and surface plasmons. In Section 6, we review recent theoretical and experimental progresses on valleytronics beyond graphene. Finally, the conclusion and perspectives are given in Section 7.

2. Valley filtering in bulk graphene monolayers

2.1. Model and formalism

Although the valley DOF is similar to the spin DOF, the role of the magnetic field in valleytronics differs greatly from that in spintronics.[66] In semiconductors with a large g factor, it is well known that electronic spin can be manipulated directly through the coupling to an external magnetic field.

The two spin components can be mixed by nonuniform magnetic fields with position-dependent orientation. In contrast, in graphene magnetic fields up to 10^4 T cannot cause a noticeable intervalley scattering. The spin–orbit interaction (SOI) in spintronics offers a way to control the spin states of charge carriers by changing their orbital motion. In graphene valleytronics, the in-plane strain and the staggered electric potential play a similar role as the SOI in spintronics.

A mechanical in-plane strain in graphene changes the hopping amplitude t into $t+\delta t(\boldsymbol{r},\boldsymbol{n})$ at the position $\boldsymbol{r}$ along a given nearest-neighbor vector $\boldsymbol{n}$. In the continuous model, its effect can be described by a gauge vector potential[9] $\boldsymbol{A}_{\rm S}(\boldsymbol{r})$. The projection of $\boldsymbol{A}_{\rm S}(\boldsymbol{r})$ along the zigzag (armchair) direction of the graphene lattice, denoted as $A_{\rm SZ}$ ($A_{\rm SA}$), can be expressed as

$$A_{\rm SZ}+{\rm i}A_{\rm SA}=\sum_{\boldsymbol{n}}\delta t(\boldsymbol{r},\boldsymbol{n})\exp(-{\rm i}\boldsymbol{K}\cdot\boldsymbol{n}), \tag{1}$$

where $\boldsymbol{K}$ is the wave vector of one Dirac point.

A bulk gap near the Dirac points was created by means of the sublattice-dependent graphene-substrate interaction.[67–72] Its size 2Δ depends on the experimental details and ranges from a few to hundreds of meV. The band gap engineering in graphene may be also realized through chemical methods.[73,74] A spatially-varying staggered potential $\Delta(\boldsymbol{r})$ was reported in Ref. [69].

Consider a bulk graphene monolayer modulated by a perpendicular magnetic field $B(\boldsymbol{r})$ (with vector potential $\boldsymbol{A}(\boldsymbol{r})$), in-plane strain, staggered potential $\Delta(\boldsymbol{r})$, and the scalar potential $U(\boldsymbol{r})$. The motion of electrons in a given valley τ ($\tau=\pm1$ for K/K' valley) can be described by the low-energy effective Hamiltonian[8]

$$H_\tau=\int{\rm d}\boldsymbol{r}\Psi_\tau^+[v_{\rm F}\boldsymbol{\sigma}\cdot(\boldsymbol{p}+e\boldsymbol{A})+\tau\boldsymbol{\sigma}\cdot\boldsymbol{A}_{\rm S}+\tau\Delta\sigma_z+U\sigma_0]\Psi_\tau. \tag{2}$$

Here $v_{\rm F}$ is the Fermi velocity, $\boldsymbol{\sigma}=(\sigma_x,\sigma_y,\sigma_z)$ is the vector formed by three Pauli matrices, $\boldsymbol{\sigma}_0$ is a unit matrix, and $\boldsymbol{p}=-{\rm i}\hbar(\partial_x,\partial_y)$ is the in-plane momentum of electrons. The valley-resolved spinor $\Psi_+=(\Psi_{\rm A},\Psi_{\rm B})^{\rm T}$ and $\Psi_-=(-\Psi'_{\rm B},\Psi'_{\rm A})^{\rm T}$ contain electron fields in two carbon sublattices A and B.

From the Hamiltonian (2) we can see that the strain term $\tau\boldsymbol{\sigma}\cdot\boldsymbol{A}_{\rm S}$ and the staggered-potential term $\tau\Delta\sigma_z$ are similar to the Rashba SOI caused by an in-plane electric field[75] in a conventional 2D electron system. They respect the time-reversal symmetry and are distinct from the term $ev_{\rm F}\boldsymbol{\sigma}\cdot\boldsymbol{A}$ caused by the magnetic field. The application of the strain or staggered potential alone can generate the valley-Hall effect,[20,41] which is the analog of the spin-Hall effect. For convenience, hereafter all quantities will be expressed in dimensionless units by means of the length scale $l_{B_0}=[\hbar/(eB_0)]^{1/2}$ and energy scale $E_0=\hbar v_{\rm F}/l_{B_0}$. For a typical magnetic field $B_0=0.1$ T, the reduced units are $l_{B_0}=81.1$ nm and $E_0=7.0$ meV.

One can set up a scattering problem from the Hamiltonian (2) and proper boundary conditions. For simplicity, we consider the case that the system has a translational invariance along a direction which is chosen as the y axis. All potentials are assumed to be uniform in the ingoing and outgoing regions. The external magnetic field is local and varies only along the x axis, which can be generated by depositing ferromagnetic metal (FM) or superconducting materials on top of the dielectric layer, as the way in semiconductor heterostructures.[76–83] The magnetic vector potential will be taken in the Landau gauge, $\boldsymbol{A}=A_y(x)\boldsymbol{e}_y$ with ${\rm d}A_y/{\rm d}x=B_z(x)$. For an electron from the valley τ incident with energy E and conserved transverse momentum $p_y=\hbar k_y$, the transmission probability $T_\tau(E,k_y)$ can be determined from its wave function

$$\Psi_\tau(\boldsymbol{r})={\rm e}^{{\rm i}k_y y}\exp\left[-{\rm i}\tau\int_{-\infty}^{x}A_{{\rm S}x}(x'){\rm d}x'\right]\psi_\tau(x,k_y). \tag{3}$$

Here the one-dimensional spinor wave function $\psi_\tau(x,k_y)$ meets $H_\tau(k_y)\psi_\tau(x,k_y)=E\psi_\tau(x,k_y)$ with

$$H_\tau(k_y)=-{\rm i}\sigma_x\partial_x+\sigma_y(k_y+A_y+\tau A_{{\rm S}y})+\tau\Delta\sigma_z+U\sigma_0. \tag{4}$$

Under the scattering boundary condition and the continuity of wave function, the transmission probability $T_\tau(E,k_y)$ can be calculated numerically by means of the scattering matrix method.[84,85]

At a low temperature $T_{\rm K}$ (in unit of $E_0/k_{\rm B}$) and Fermi energy $E_{\rm F}$, the valley-resolved ballistic conductance $G_\tau(E_{\rm F})$ can be expressed in terms of the transmission probability $T_\tau(E,k_y)$,

$$G_\tau(E_{\rm F})=G_0\int{\rm d}E\frac{-\partial f}{\partial E}\int_{-\infty}^{+\infty}T_\tau(E,k_y)\frac{{\rm d}k_y}{2\pi/L_y}, \tag{5}$$

where $G_0=e^2L_y/(2\pi^2\hbar l_{B_0})$ is taken as the conductance unit, L_y is the sample size along the y direction, and $f(E)=\{1+\exp[(E-E_{\rm F})/T_{\rm K}]\}^{-1}$ is the Fermi–Dirac distribution function. The valley polarization is defined as

$$P=\frac{G_K-G_{K'}}{G},\quad G=G_K+G_{K'}. \tag{6}$$

2.2. Symmetry analysis

In the absence of magnetic barrier, the Hamiltonian (4) satisfies[17]

$$\sigma_x H_\tau(k_y)\sigma_x^{-1}=H_{-\tau}(-k_y), \tag{7}$$

which indicates $T_\tau(E,k_y)=T_{-\tau}(E,-k_y)$. This together with Eq. (5) results in a vanishing valley polarization P. Thus the elastic deformation or staggered potential alone can not produce a valley polarization in two-terminal graphene devices. The inclusion of a magnetic barrier is necessary to obtain a valley-polarized current from the considered system.

For unstrained graphene under a uniform staggered potential, a finite valley polarization requires not only magnetic barriers but also electric barriers.[49] This can be readily seen from the equation that the two components of the spinor ψ_τ satisfy

$$[\partial_x^2 + F_0^{\pm} + F_\tau^{\pm}(\pm k_y \pm A_y - \partial_x)]\psi_{\tau\pm} = 0, \tag{8}$$

$$F_\tau^{\pm} = (E - U \pm \tau\Delta)^{-1}(\pm\tau\partial_x\Delta - \partial_x U), \tag{9}$$

$$F_0^{\pm} = (E-U)^2 - \Delta^2 - (k_y + A_y)^2 \mp \partial_x A_y. \tag{10}$$

In the case $\partial_x\Delta = 0$ and $\partial_x U = 0$, F_τ vanishes and Eq. (8) becomes valley-independent. Accordingly, no valley polarization can be produced.

Valley filtering also disappears when A_y, U, and Δ are symmetric (while A_{Sy} is zero or antisymmetric) with respect to the center line $x_c = L/2$ of the scattering region. In this case, the reflection operation $R_x : x \to 2x_c - x$ together with σ_y transforms the Hamiltonian H_+ into H_-, i.e.,

$$\sigma_y R_x H_+(k_y)\sigma_y R_x = H_-(k_y). \tag{11}$$

If $\psi_+(x,k_y)$ is a scattering eigenstate of Eq. (4) for K electrons incident from one side of the scattering region, then $\psi_-(x,k_y) = \sigma_y\psi_+(L-x,k_y)$ is also a solution of Eq. (4) but for K' electrons incident from the opposite side. The transmission through a single-channel scattering potential is irrelevant to the incident directions because of the unitary of the scattering matrix. These two facts tell us that the transmission probability is also valley-independent and satisfies[50]

$$T_\tau(E,k_y) = T_{-\tau}(E,k_y). \tag{12}$$

In the case that A_y and A_{Sy} are antisymmetric while U and Δ are symmetric (with respect to $x = x_c$), the transmission spectrum of either valley electron shows a mirror symmetry about $k_y = 0$, i.e., $T_\tau(E,k_y) = T_\tau(E,-k_y)$. For $A_y = A_{Sy} = 0$, this mirror symmetry holds for any U and Δ.

3. Valley filtering in strained graphene

3.1. Strained graphene under a magnetic barrier

We demonstrate that the combination of a magnetic barrier and in-plane strain can generate a finite valley polarization[17] in a two-terminal graphene device (see Fig. 1(a)). A simplified strain profile[86] is taken to create a uniform perturbation $\delta t \equiv A_S$ of the hopping along the x direction, over a region $x \in [0, L_S]$. Such a strain can be induced by a uniform tension along the x direction applied on the substrate.[87] The strain with amplitude $\approx |\delta t|/(2.7\,\text{eV})$ up to 15% affects insignificantly the graphene band structure.[88] The magnetic barrier is created by an FM stripe with magnetization along the x direction and at a distance D to the strained region. The corresponding vector potential is approximated as a rectangular shape with width L_M and height A_M. The distributions of the total (dimensionless) vector potential $A_y(x) = A_M(x) + A_S(x)$ for the two valleys are shown in Fig. 1(b). The scalar potential U is U_S (U_M) in the strain (magnetic barrier) region and zero otherwise. Note that U_M can be tuned by the voltage applied on the FM stripe.

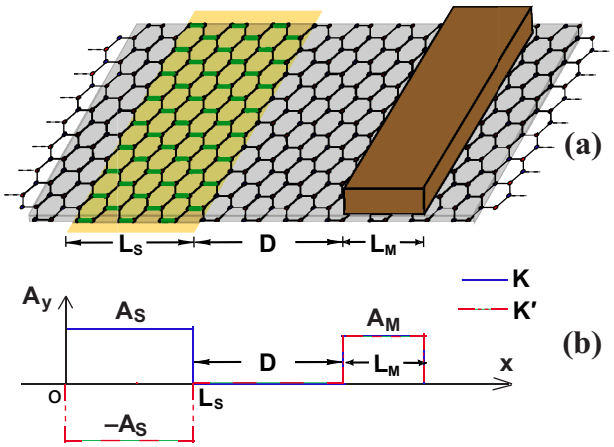


Fig. 1. (a) Schematic of a graphene valley filter with a dielectric layer and a substrate strain (the yellow shaded region with thicker bonds). An FM stripe with magnetization along the transporting x direction is deposited on the dielectric layer to create a magnetic barrier. (b) Profile of the total vector potential $A_y(x)$ for electrons in the K and K' valleys. Electrons with valley index τ feel the strain-induced vector potential τA_S in the region $0 < x < L_S$ and magnetic-barrier-induced vector potential A_M in the region $L_S + D < x < L_S + D + L_M$. Reproduced with permission from Ref. [17].

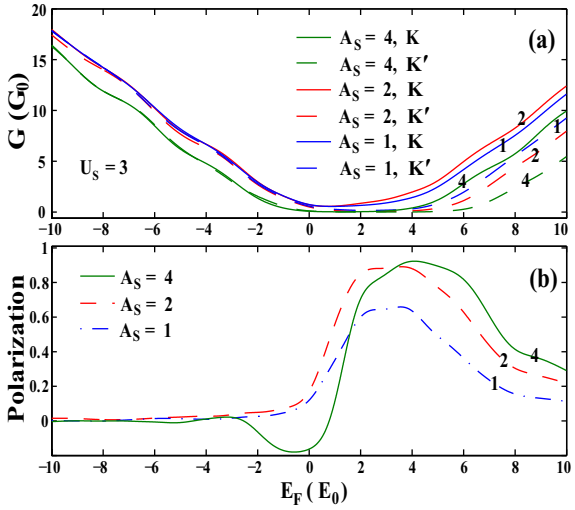


Fig. 2. Valley-dependent conductance (a) and valley polarization (b) for the valley filter in Fig. 1(a) plotted as a function of the Fermi energy E_F at a given temperature $T_K = 0.5$ and height of the scalar potential $U_S = 3$. The amplitude of strain-induced vector potential A_S is marked in each curve. Reproduced with permission from Ref. [17].

In the numerical calculations, we take the structural parameters as $L_M = L_S = D = 1$ and set $A_M = 2$ and $U_M = U_S$. The transmission $|t_\tau|^2$ exhibits a strong anisotropy of incident angle and resonant tunneling, which leads to a rich oscillation feature in the zero-temperature conductance spectrum (not shown here). At a relatively high temperature $T_K = 0.5$

the oscillations are washed out, as shown in Fig. 2. One can see that for $E_F > U_S$ the conductance G_K is usually larger than $G_{K'}$. This can be understood from the shifts of the Dirac point in the magnetic barrier and the strain region, δk_M and δk_S, which are in the same (opposite) direction for the K (K') valley (see Fig. 1(b)). There are more available open transmission channels for the parallel shift ($\delta k_M \cdot \delta k_S > 0$) than that for the antiparallel shift. There exists a broad energy region where G_K is finite while $G_{K'}$ is rather small. Accordingly, one can achieve a valley polarization exceeding 80% together with a remarkable total conductance (Fig. 2(b)). Similar to the spin current, the valley current in the linear-response regime is characterized by $\Delta G = G_K - G_{K'}$. In the high Fermi energy region, ΔG varies slowly with E_F while P decreases monotonically.

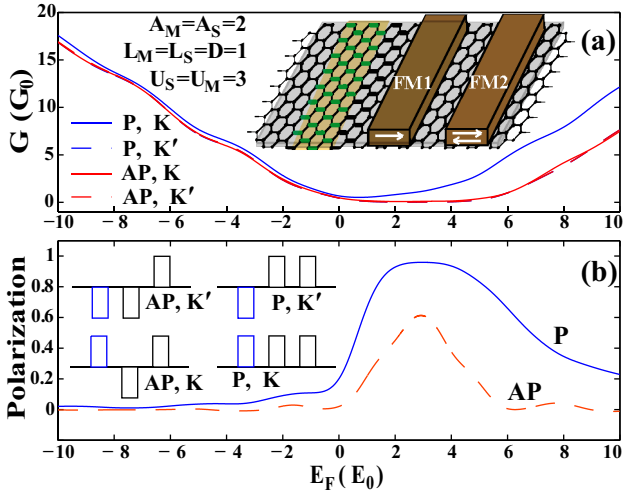


Fig. 3. Valley-dependent conductance (a) and valley polarization (b) plotted as a function of the Fermi energy E_F at a given temperature $T_K = 0.5$ for the device illustrated in the inset of panel (a). The inclusion of another FM stripe transforms the system shown in Fig. 1(a) to a valley filtering switch. The inset in panel (b) plots the profiles of the total vector potential $A_y(x)$ for the K and K' electrons and for the parallel and antiparallel magnetization configurations of the two FM stripes. The width of each region (L_S and L_M) and the distance D between adjacent regions are taken as 1 while the height of the vector (scalar) potential in each region is set at $A_S = A_M = 2$ ($U_S = U_M = 3$).

Based on the operating principle of this valley filter, one can design a valley filtering switch[18] depicted in the inset of Fig. 3(a). Now the local magnetic field is created by two parallel FM stripes (FM1 and FM2) with magnetization along the $\pm x$ or direction. When their magnetizations are switched from the parallel (P) to the antiparallel (AP) alignment, the valley polarization P and ΔG change greatly in a wide range of E_F (see Fig. 3). Actually, ΔG is rather small for the AP alignment in the whole considered energy region. The reason is that in this case the number of open channels for K electrons is almost the same as that for the K' electrons (see the profiles of the total vector potential in the inset of Fig. 3(b)). Based on the same reason, the conductance G_τ for the P alignment differs slightly from that for the device in Fig. 1(a) in the case $A_S = A_M$. A large valley polarization or a notable ΔG thus can be achieved in this magnetization configuration. We can even design a valley-related logic AND device[18] based on smooth potentials under realistic parameters, which is the same as that in Fig. 3(a) but with many parallel FM stripes like FM2. The device is in a low-resistance state if the magnetizations of all FM stripes are in parallel and in a high-resistance state otherwise. Only in the low-resistance state can the device output a remarkable valley current.

The valley polarization in the strained graphene can be enhanced by the application of a finite magnetic superlattice.[19] The coexistence of insulating transmission gap of one valley and metallic resonant band of the other results in a substantial current with full valley polarization. The fully valley-polarized current appears in a wide range of edge orientation and temperature, and can be effectively tuned by structural parameters. The valley filtering of massless Dirac Fermions was also studied[89] in 2D materials with a tilt Dirac cone (such as 8-*Pmmn* borophene[90]). When the magnetic–electric barrier provided by a single FM gate is perpendicular to the tilted direction of the Dirac cone, one can yield a nearly perfect valley polarization for a realistic magnetic barrier. Due to intrinsic symmetry, the valley polarization vanishes when the barrier orientation is along the tilted direction. The tilting of Dirac cones is essential for the anisotropic valley filtering. It seems that the tilt term plays the role of strain-induced pseudo-vector potential $\boldsymbol{A}_S$ in graphene. The component of $\boldsymbol{A}_S$ along the transport direction can be eliminated[17] by a local unitary transformation (see Eqs. (3) and (4)). In contrast, the tilt term affects the transmission for all transport directions. This comparison indicates the difference between the tilt term and $\boldsymbol{A}_S$.

3.2. Goos–Hänchen shift in strained graphene

From the symmetry analysis, the elastic deformation alone cannot produce a valley polarization in two-terminal graphene devices when valley-unpolarized electrons incident from all directions are detected. This constraint may be circumvented by either collecting part of the output current or injecting a collimated electron beam, as the way in two proposed spin-filter devices[91,92] utilizing only the SOI.

Electrons ballistically propagating in graphene have deep analogies with light because of the massless linear dispersion and the chirality. Electronic analogies of optical phenomena such as reflection, refraction, polarization, focusing, and collimation inspired several graphene-based proposals such as the Veselago lens and spin lenses.[93,94] A well-known wave effect in optics is the Goos–Hänchen (GH) shift,[95] which is the lateral shift of a totally reflected beam of light with respect to the position predicted by geometrical optics. In graphene p–n–p junctions, the GH effect of Dirac electrons was predicted to result in an $8e^2/h$ conductance plateau.[96]

To discuss valley filtering based on optical-like behaviors of Dirac electrons, we consider an interface in graphene separating an unstrained normal (N) region and a strained (S) region (Fig. 4(a)). A constant gauge potential $A_S > 0$ and electric potential U_S exist in the S region. A valley-unpolarized beam ψ_{in} with energy E is incident from the N region. It is assumed to be well-collimated[97,98] around an angle $\theta_N = \arcsin(k_y/E)$, i.e.,

$$\psi_{in}(x,y) = \int e^{ik'_y y}\psi_N(x;k'_y)f(k'_y - k_y)\,dk'_y, \tag{13}$$

$$\psi_N(x;k_y) = e^{ik_0(x-x_N)}\,[1,(k_0+ik_y)/E]^T/\sqrt{2}, \tag{14}$$

where the profile of the beam is taken as a Gaussian with width Δ_q, i.e., $f(q) = \exp[-q^2/(2\Delta_q^2)]$, and $k_0 = \mathrm{sgn}(E)\sqrt{E^2 - k_y^2}$. The incident beam has a central position y_{in} at the N/S interface $x_N = 0$.

An electron in the beam center and from the τ valley will transmit partly into the S region with the refraction angle[25]

$$\theta_{S\tau}(\theta_N) = \arcsin[(E\sin\theta_N + \tau A_S)/(E - U_S)]. \tag{15}$$

It is partly reflected into the N region with reflection amplitude

$$r_\tau^{NS} = \frac{\exp(i\theta_{S\tau}) - \exp(i\theta_N)}{\exp(-i\theta_{S\tau}) + \exp(i\theta_N)}. \tag{16}$$

Figure 4(b) shows the refraction angle $\theta_{S\pm}$ as a function of the incident angle θ_N for the simplest case $U_S = 0$. For normal incidence, the two refraction angles satisfy $\theta_{S+} = -\theta_{S-} \neq 0$. This valley beam splitting is distinct from the optical double refraction in uniaxial crystals and the SOI-induced beam splitting in semiconductor heterostructures.[92] The angular separation of the two refraction beams, $\Delta\theta_S = |\theta_{S+} - \theta_{S-}|$, increases with $|\theta_N|$ and can be controlled by the strain strength.

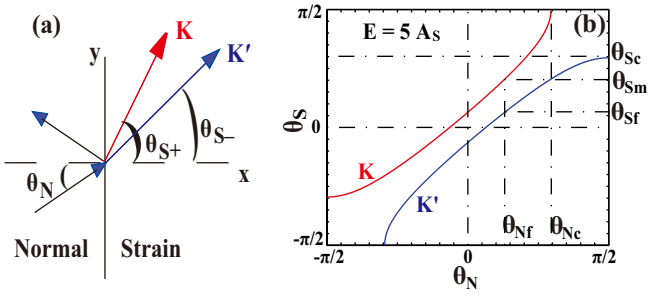


Fig. 4. (a) Schematic of valley double refraction of Dirac electrons in graphene at a N/S interface. The incident beam is valley-unpolarized. (b) Refraction angle $\theta_{S\pm}$ plotted as a function of the incident angle θ_N for incident energy $E = 5A_S$ (A_S is the amplitude of strain-induced vector potential) and scalar potential $U_S = 0$. Reproduced with permission from Ref. [25].

The characteristic angles marked in Figs. 4(b) are related to valley filtering. θ_{Sc} is the maximal outgoing angle of K' electrons. One will obtain a fully valley-polarized current if electrons are collected only in the angle interval $(\theta_{Sc}, \pi/2)$. Valley double refraction happens for $\theta_N \in (-\theta_{Nc}, \theta_{Nc})$, where θ_{Nc} is the critical incident angle for total reflection of K electrons. To achieve a valley beam splitter, one can restrict the incident angle to be within an interval $(\theta_{Nf}, \theta_{Nc})$ so that K electrons are scattered into the angle interval $(\theta_{Sm}, \pi/2)$ while K' electrons are scattered into the angle interval $(\theta_{Sf}, \theta_{Sm})$. Here $\theta_{Sm} = \theta_{S-}(\theta_{Nc}) = \theta_{S+}(\theta_{Nf})$ is the separation angle of two valley-polarized beams, which is negative for $1 < (E - U_S)/A_S < 2$.

At the interface $x = x_N$, the central position of the reflected beam for τ electron differs from y_{in}. Their difference is the valley-resolved GH shift[96]

$$\sigma_{r\tau}^{NS} = -\mathrm{Im}\frac{\partial \ln r_\tau^{NS}(E,k_y)}{\partial k_y} + \frac{\partial\theta_N}{\partial k_y}. \tag{17}$$

In the case of total reflection ($\mathrm{Im}\theta_{S\tau} \neq 0$), one gets[26]

$$\sigma_{r\tau}^{NS} = \frac{2k_y + \tau A_S}{k_0|(E - U_S)\cos\theta_{S\tau}|}. \tag{18}$$

The GH shift $\sigma_{r\tau}^{NS}$ can be utilized to construct a valley-filtered graphene guiding device depicted in Fig. 5(a). In the device, the middle waveguide is unstrained and sandwiched by two strained regions. When electrons are incident into the waveguide with incident angle $\theta_N > \theta_{Nc}$, the GH shifts at each N/S interface accumulate during all reflection processes. Under this condition, guiding modes may be formed in the waveguide.[99] A semiclassical analysis[96] revealed that the GH shift $\sigma_{r\tau}^{NS}$ can change the propagating velocity $v_\parallel$ of electrons along the waveguide. The presence of guiding modes requires the decrease of $v_\parallel$, which depends on the valley index.

The dispersion relation $E(k_y)$ of guiding modes can be calculated numerically from a tight-binding model, which is plotted in Fig. 5(b) (red lines). The dispersion relation satisfies $E(k_y) = E(-k_y)$ and has particle–hole symmetry. For the considered parameters, forward-going guiding modes with $0 < E < 3$ eV exist only for K' electrons. The density distribution of the two lowest forward-going modes with $k_y = -0.60|\boldsymbol{K}|$ are shown in Fig. 5(c). These guiding modes in K' valley and corresponding bulk modes in K valley are well separated spatially in the lateral direction. One can connect the strained graphene ribbon to two wide leads (from upper and lower) and calculate the ballistic conductance. The conductance shown in Fig. 5(d) follows the number of guiding modes rather than the number of transmission modes in leads. Electrons leak out of the waveguide can be sinked by two electrical grounds G1 and G2 on the strained regions. Then the guiding modes will dominantly carry fully valley-filtered current from the injector to the collector.

The valley double refraction at a N/S interface serves as a basis for creating valley-splitting beams in another unstrained region O, as depicted in the inset of Fig. 6(a). The transmitted

beam $\psi^{\tau}_{\rm out}(x,y)$ is formed by τ electrons traversing the middle S region with transmission amplitude $t_\tau(E,k_y)$. The exiting position of this beam at the S/O interface $x_{\rm O}=L_{\rm S}$ becomes $y^{\tau}_{\rm out}=y_{\rm in}+\sigma_\tau$. For a narrow beam with $\Delta_{\rm q}\ll|E|$, the stationary-phase approximation[100] gives the formula of the GH shift for the transmitted beam[25]

$$\sigma_\tau(E,\theta_{\rm N})=-{\rm Im}\frac{\partial \ln t_\tau(E,k_y)}{\partial k_y}. \tag{19}$$

One can place a detector to collect only the K (K') electrons, whose position depends on the valley spatial separation

$$D=|y^{+}_{\rm out}-y^{-}_{\rm out}|=|\sigma_+-\sigma_-|. \tag{20}$$

The GH shift σ_τ is generally unequal to the classical result $\sigma^{\rm cl}_{\pm}=L_{\rm S}\tan\theta_{\rm S\pm}$ and thus the wave effect should be considered. At a resonant incident angle $\theta^{\rm res}_{\rm N}$, we obtain the expression for the lateral displacement

$$\sigma^{\rm res}_\tau=F_0L_{\rm S}\tan\theta^{\rm res}_{\rm S\tau},\quad F_0=\frac{1-\sin\theta^{\rm res}_{\rm N}\sin\theta^{\rm res}_{\rm S\tau}}{\cos\theta^{\rm res}_{\rm N}\cos\theta^{\rm res}_{\rm S\tau}}. \tag{21}$$

The magnified factor F_0 equals approximately the peak-to-trough ratio of the transmission resonance.

The angular dependence of $\sigma_\pm$ is shown in Fig. 6(a) for a strained graphene n–n′–n junction where valley double refraction occurs for all incident angles. The valley spatial separation D can exceed $D^{\rm cl}=|\sigma^{\rm cl}_+-\sigma^{\rm cl}_-|$ greatly at large $|\theta_{\rm N}|$ whereas the transmitted beam may be difficult to detect. For strained graphene n–p–n junctions (Figs. 6(b) and 6(c)), negative refraction occurs for K electrons ($\sigma^{\rm cl}_+<0$). It can be seen from Figs. 6(c) and 6(d) that the maximum of $|\sigma_\tau|$ appears at resonant incident angles. Around the transmission peaks of K electrons with a large F_0, σ_- is almost the same as $\sigma^{\rm cl}_-$. Accordingly, the valley spatial separation D can be enhanced at the transmission resonance.

For a typical tilted Dirac system (8-*Pmmn* borophene), the valley-resolved lateral shift of electrons traversing an n–p–n junction was studied theoretically.[101] We derive a gauge-invariant formula on the GH shift of transmitted beams, which holds for any anisotropic isoenergy surface. Due to the similarity between the tilting effect of the Dirac cone and strain-induced vector potential in graphene, valley double refraction also occurs at the considered n–p interface. The valley spatial separation D can be enhanced to be ten to hundred times larger than the barrier width. However, D is always zero when the junction is along the tilt direction of Dirac cones.

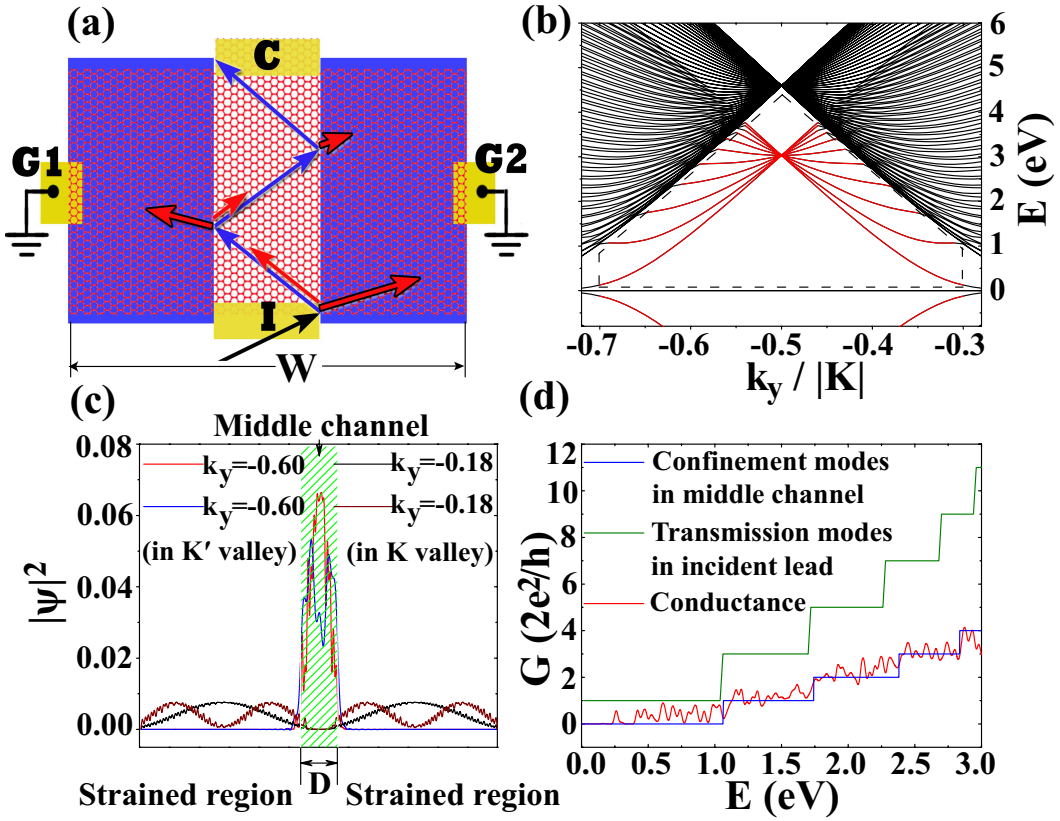


Fig. 5. (a) Schematic of a graphene guiding device with strain in shaded regions. It includes an injector (I), a collector (C), and two electrical grounds (G1 and G2). The black and red/blue arrows denote the unpolarized incident electron beam and K/K'-valley-polarized propagating beams. (b) Energy dispersion near $k_y=-0.5|\boldsymbol{K}|$ of the graphene ribbon in panel (a) consisting of $W=61$ zigzag chains. Outside the unstrained region with $D=6$ zigzag chains, the hopping variation induces a strain of $\sim 10\%$. (c) Density distributions of the lowest two forward-going modes with $k_y=-0.60|\boldsymbol{K}|$ in K' valley and $k_y=-0.18|\boldsymbol{K}|$ in K valley. (d) Conductance G, number of propagating modes in the channel and in the lead plotted as a function of incident energy E. Reproduced with permission from Ref. [26].

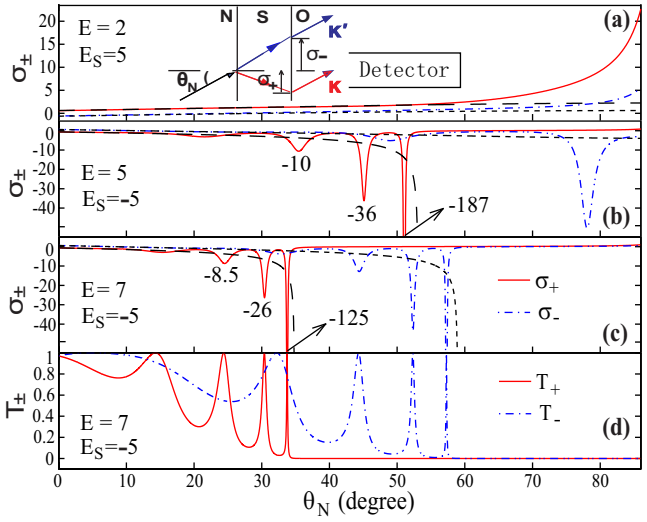


Fig. 6. (a)–(c) Valley-resolved GH shift σ_+ (red solid lines) and σ_- (blue dash-dotted lines) together with their classical values $\sigma_\pm^{\rm cl}$ (black dashed lines) and $\sigma_-^{\rm cl}$ (black dotted lines) plotted as a function of the incident angle $\theta_{\rm N}$. (d) Valley-resolved transmission probability versus incident angle. Some values of the resonant GH shift for K electrons are marked in panels (b) and (c). The values of incident energy E and $E_{\rm S}=E-U_{\rm S}$ ($U_{\rm S}$ is the height of the scalar potential) are given in each panel. The pseudo-vector potential has amplitude $A_{\rm S}=1$ in the S region with width $L_{\rm S}=3$. The inset in panel (a) depicts schematically the lateral displacements $\sigma_\pm$ of transmitted electron beams $\psi_{\rm out}^{(\tau)}(L,y)$. A detector placed in the outgoing region can collect only the K (K') electrons. Reproduced with permission from Ref. [25].

4. Valley filtering in gapped graphene

4.1. Gapped graphene under a magnetic barrier

For many proposed valley filters, the detection of the generated valley polarization requires additional elaborate setup. It was shown theoretically that in graphene with broken inversion symmetry, the injection of valley-polarized current will generate a transverse voltage,[41] in a similar way as inverse spin-Hall effect.[102,103] Valley filters based on gapped graphene thus could be integrated with valley detectors. We demonstrated that for a two-terminal graphene system with a Dirac gap, a proper magnetic–electric barrier provided by a single FM gate can produce a remarkable valley polarization.[49]

The considered graphene system is illustrated in Fig. 7(a), where a Dirac gap 2Δ is created by means of substrate engineering. A single FM gate together with a dielectric spacer is deposited on top of graphene. The FM gate has a rectangular cross section (see Fig. 7(a)) with width $L_{\rm F}$ and a magnetization $\boldsymbol{M}$ along the z axis.[77,80,81] The obtained magnetic–electric barrier can be simplified as a rectangular shape, i.e., $B(\boldsymbol{r})=B_{\rm s}\Theta(x)\Theta(L_{\rm F}-x)$ and $U(\boldsymbol{r})=U_{\rm s}\Theta(x)\Theta(L_{\rm F}-x)$. Here $\Theta(x)$ is the Heaviside step function, and $B_{\rm s}\neq 0$ and $U_{\rm s}$ are constant. We obtain an analytical expression[49] of the transmission $T_\tau(E,k_y)$ from Eq. (4), which depends on the valley index only through the parameter γ_τ defined by

$$\gamma_\tau=\sqrt{2B_{\rm s}}(E+\tau\Delta)/(E+\tau\Delta-U_{\rm s}). \tag{22}$$

The transmission probability is plotted in Fig. 7 as a function of k_y for a typical incident energy $E=7$, Dirac gap $2\Delta=8$, and width $L_{\rm F}=2$. All transmission curves exhibit a mirror symmetry about $k_y=0$, which results from the symmetry of the considered structure. Pronounced resonances appear in the case of interband tunneling ($U_{\rm s}>2\Delta$). They stem from the quasibound states in the barrier region. It was shown that[104] a uniform magnetic field can lift the valley degeneracy of quantum dots formed electrostatically in gapped graphene. When $B_{\rm s}\neq 0$, the quasibound states discussed here have a similar valley-splitting, leading to a valley-dependent resonant enhancement and suppression. The valley contrast of the transmission in interband tunneling is more remarkable than that in intraband tunneling ($U_{\rm s}<0$). This observation is due to the dependence of $\gamma_\pm$ (Eq. (22)) on the electric barrier. Since the area under the T_τ–k_y curve is proportional to the conductance G_τ (Eq. (5)), the valley-dependent transmission shown in Figs. 7(c)–7(e) results in a finite valley polarization.

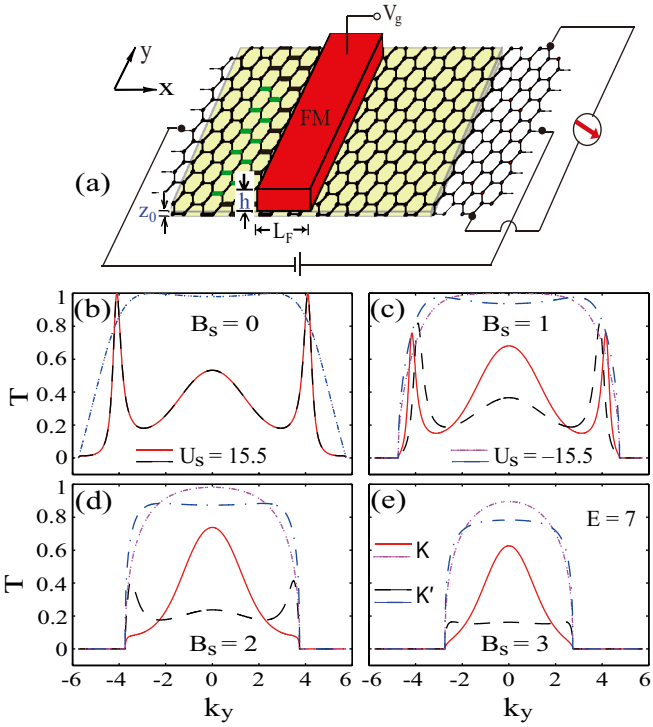


Fig. 7. (a) Valley filter based on gapped graphene modulated by the magnetic–electric barrier provided by a single FM gate with height h, width $L_{\rm F}$ and distance z_0 to the graphene plane. The generated valley polarization can be detected by the inverse valley-Hall effect. (b)–(e) Valley-resolved transmission T_+ and T_- as a function of the wave vector for electrons traversing a square magnetic–electric barrier with height of electric barrier $U_{\rm S}=\pm 15.5$ and amplitude of magnetic field $B_{\rm S}=0$, 1, 2, and 3. Other parameters are: the incident energy $E=7$, the barrier width $L_{\rm F}=2$, and the Dirac gap $2\Delta=8$. Reproduced with permission from Ref. [49].

When the magnetization of the FM gate in Fig. 7(a) changes to the current direction, an antisymmetric magnetic barrier is obtained, which together with a symmetric electric potential can not generate a valley-polarized current.[50] In this situation, the system is invariant under the operation $\sigma_y R_x$. One can break this symmetry by placing a normal-metal

(NM) gate (with width $L_{\rm N}$) parallel to the FM gate, as shown in Fig. 8(a). The antisymmetric magnetic barrier leads to a valley-dependent change of the reflection phase, which is utilized to create a valley contrast of transmission probability by the inclusion of an electric barrier. For a realistic smoothing profile of potentials, the valley-resolved conductance and valley polarization are plotted in Fig. 8 as a function of the potential height of the NM gate. The FM gate has a height $h = 0.6$, magnetization $\mu_0 M_x = 1.8$ T (for cobalt material), and a distance $z_0 = 0.3$ to the graphene plane.

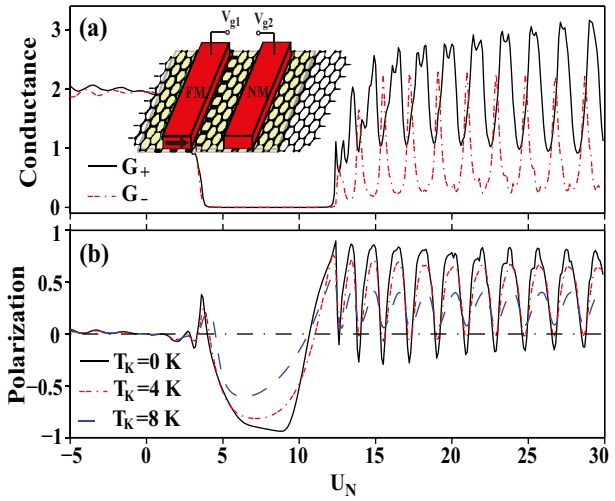


Fig. 8. (a) Valley-resolved zero-temperature conductance $G_\pm$ and (b) valley polarization P as a function of the barrier height $U_{\rm N}$ (controlled by the NM gate) under different temperatures $T_{\rm K} = 0$, 0.05 and 0.1 (0 K, 4 K, and 8 K). The inset in panel (a) depicts the proposed valley filter based on a gapped graphene with an FM gate and an NM gate on top. The FM gate has a rectangular cross section and a magnetization along the current direction. We set $E_{\rm F} = 8$ and the barrier height $U_{\rm F} = 20$ (controlled by the FM gate). Reproduced with permission from Ref. [50].

Under the setting $U_{\rm F} = 20$ and $E_{\rm F} = 8$, interband tunneling happens in the region covered by the FM gate. When $U_{\rm N} > E_{\rm F} + \Delta$, one can see regular oscillations in the conductance spectrum. Significant valley polarization can be achieved at zero temperature when the maximum of G_+ is near a minimum of G_-. A finite temperature reduces the valley polarization. At the temperature $T_{\rm K} = 0.05$ (4 K) the valley polarization still has remarkable maximums and minimums close to zero. Therefore, in the low-temperature regime the valley polarization is remarkable and can be tuned by voltages on the NM gate.

4.2. Valley-Zeeman effect

In gapped graphene with a broken inversion symmetry, Berry curvature and orbital magnetic moment (OMM) are finite and can be used to distinguish valley states.[41] Berry curvature describes the geometric characteristics of the electronic energy bands, while the OMM results from the rotation of the wave packet of Bloch electrons around its center. For the Hamiltonian in Eq. (2) without external fields, the Berry curvature $\boldsymbol{\Omega}$ and OMM $\boldsymbol{m}$ are along the z axis. Their z components are given by

$$\Omega_z(\boldsymbol{k}) = -\tau v_{\rm F}^2 \hbar^2 \Delta/(2[E(\boldsymbol{k})]^3), \tag{23}$$

$$E(\boldsymbol{k}) = \pm\sqrt{(\hbar v_{\rm F}\boldsymbol{k} + \tau \boldsymbol{A}_{\rm S})^2 + \Delta^2}, \tag{24}$$

$$m_z(\boldsymbol{k}) = [\Delta/E(\boldsymbol{k})]^2 m_{z0}, \tag{25}$$

$$m_{z0} = -\tau e \hbar v_{\rm F}^2/(2\Delta). \tag{26}$$

Here the energy $E(\boldsymbol{k})$ is positive (negative) for electrons in the conduction (valence) band. Both $\Omega_z(\boldsymbol{k})$ and $m_z(\boldsymbol{k})$ are opposite in the two valleys, which respects the time-reversal symmetry. For $v_{\rm F} \approx 10^6$ m/s and $\Delta \approx 50$ meV, one can estimate $|m_{z0}| \approx 114\mu_{\rm B}$, where $\mu_{\rm B} = 5.788 \times 10^{-2}$ meV/T is the Bohr magneton.

The Berry curvature can be viewed as another pseudomagnetic field, which presents in the momentum space and brings a valley-dependent anomalous velocity[41] of electrons. Therefore, the application of an in-plane electric field can generate a transverse pure valley current. This phenomenon is called the valley Hall effect, which is similar to the spin Hall effect in 2D electron systems with spin–orbit coupling.[66] By aligning graphene with an underlying layer of hexagonal boron nitride, Gorbachev *et al.*[105] reported the long-range character and transistor-like gate control of valley Hall currents. In Ref. [106], pure valley current was generated in dual-gated bilayer graphene and detected by nonlocal resistance measurements.

The finite OMM can be manifested by external magnetic fields through the valley-Zeeman coupling[107–110]

$$\hat{H}^{\rm VZ} = \tau U_{\rm m}\hat{\sigma}_0, \quad U_{\rm m} = B_z|m_{z0}|F\left(\left|\frac{E}{\Delta}\right|\right), \tag{27}$$

$$F(X) = X^{-2}\Theta(X-1). \tag{28}$$

The valley-splitting energy $2|U_{\rm m}|$ depends on the energy E of electron states, gap 2Δ, and vertical component B_z of the magnetic field. The valley g factor $g_{\rm v} = 2|U_{\rm m}/(\mu_{\rm B}B_z)|$ was measured in graphene bilayer[107] and trilayer.[108] For a quantum point contact in bilayer graphene, Lee *et al.*[107] used the finite bias spectroscopy to measure the energy spectrum due to the lateral confinement and Zeeman splitting. They reported a spin g factor of about 2 and a gate-tunable valley g-factor ranging from 40 to 120. Ge *et al.*[108] studied the gate and sublattice-resolved scanning tunneling spectroscopy for Bernal-stacked graphene trilayer under perpendicular electric and magnetic fields. They demonstrated a large and tunable valley g-factor up to 1050.

Based on the valley-Zeeman coupling (27) and gate-tunable band gap in bilayer graphene, Park *et al.*[109] proposed a valley filter and valley valve device. The valley filter is made of a n–p–n (or p–n–p) junction subject to a vertical magnetic field. The valley valve is realized in another junction, where

the gate voltage is changed to tune the size of the energy gap. They demonstrate numerically a nearly perfect valley polarization and high efficiency of the valley-valve effect.

4.3. Valley filtering due to magnetic proximity

Pristine graphene stands as a promising spin-channel material.[9] The exchange–proximity interaction[111–115] provides a way to design graphene-based spin-logic devices. The magnetism in graphene is introduced by the hybridation between the p_z orbitals of electrons in graphene and the d or f orbitals of neighboring magnetic ions in a ferromagnetic insulator (FI) or ferrimagnet. For graphene under the magnetic proximity, quantized anomalous Hall effect[112] and accompanying high mobility were reported, while giant proximity magnetoresistance,[115–117] and chiral charge pumping[118] were predicted.

For electrons in graphene under magnetic proximity, the effective Hamiltonian[119] around the K and K valleys includes not only the exchange splitting, but also a spin-dependent Fermi velocity and gap opening. The model parameters saturate for FI film with a thickness of several layers. The stray field emanated from the FI modulates the motion of electrons in graphene. It can couple with the OMM, leading to a valley-Zeeman coupling. We study the valley-dependent electron transport properties of graphene in proximity to the FI EuO.[62] A metallic gate on top of the thick EuO layer is used to create an electrostatic potential with height U_F.

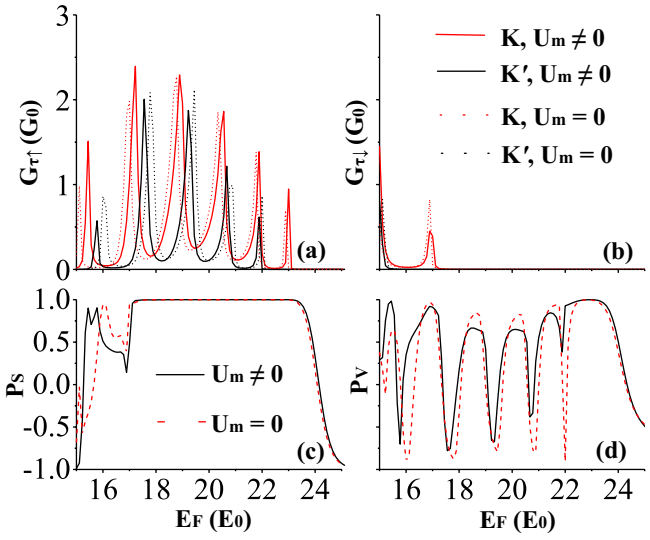


Fig. 9. Conductance and polarization plotted as functions of Fermi energy E_F (a) and (b) valley-resolved conductances $G_{\tau\uparrow}$ and $G_{\tau\downarrow}$ for spin-up and spin-down electrons. (c) Spin polarization $P_S = (G_{+\uparrow} + G_{-\uparrow} - G_{+\downarrow} - G_{-\downarrow})/(G_{+\uparrow} + G_{-\uparrow} + G_{+\downarrow} + G_{-\downarrow})$. (d) Valley polarization $P_V = (G_{+\uparrow} + G_{+\downarrow} - G_{-\uparrow} - G_{-\downarrow})/(G_{+\uparrow} + G_{-\uparrow} + G_{+\downarrow} + G_{-\downarrow})$. The calculations are made in the presence ($U_m \neq 0$) or absence ($U_m = 0$) of the valley-Zeeman coupling given by Eq. (27). Reproduced with permission from Ref. [62].

In the case of interband tunneling (at a large U_F), the spin and valley-related conductance is plotted in Fig. 9. The spin-up conductance shows several valley-resolved peaks with a large peak-to-trough ratio. The spin-down conductance is mainly contributed by the K branch and is remarkable only for E_F near U_F. Consequently, spin-resolved valley filtering can be achieved in graphene by magnetic proximity. In this situation, the valley-Zeeman splitting can change greatly the spin and valley polarization. In the case of intraband tunneling, our numerical results indicate that the valley-Zeeman coupling plays a minor role, although both the spin and valley polarization can approach -100% in a window of Fermi energy.

5. Valley-related collective motions

5.1. Valley-polarized edge plasmons

In a 2D material, charges accumulated near its edges can oscillate collectively. Subsequently, a distinct plasmon mode called edge plasmon arises, where the accompanied electromagnetic fields are localized near the edges and have a stronger confinement than those for surface plasmons. Edge plasmons were first observed experimentally in a bounded 2D electron gas[120] subject to a perpendicular external magnetic field (named edge magnetoplasmons). For edge magnetoplasmons in a graphene disk, Kumada *et al.*[121] measured the dispersion relation and decay time. Owing to the linear and gapless band structure of graphene, the dissipation of edge magnetoplasmons in graphene was indicated to be lower than that in conventional 2D systems. For a 2D electron system modulated by opposite magnetic domains, a new type of one-way edge magnetoplasmons was predicted,[122] which is topologically analogous to the zero modes of a 2D topological $p + ip$ superconductor.

In strained graphene, due to the presence of strain-induced pseudomagnetic field, edge plasmons can be formed without external magnetic fields. A uniform pseudomagnetic field up to hundreds of Tesla[20] can be achieved by designed strains in graphene. For graphene grown on a platinum surface, Levy *et al.*[123] reported that the highly strained nanobubbles therein lead to Landau levels due to pseudomagnetic fields in excess of 300 T. Giant pseudo-magnetic fields up to 800 T were reported recently by placing strain-free monolayer graphene on architected nanostructures.[124] This nanoscale strain engineering at room temperature paved a pathway toward scalable graphene-based valleytronics. Recently, Principi *et al.*[30] predicted that two counterpropagating acoustic plasmons exist at the edge of a strained graphene system. Note that electrons in the two valleys are always electrostatically coupled. In the limit of strong pseudomagnetic field, they found that the excited plasmon is valley-polarized, i.e., is contributed mainly by electrons from a specific valley. In Ref. [30], the Navier–Stokes equations for electron velocities in two valleys were linearized to yield an analytical solution. With the pseudomagnetic field increasing, the calculated val-

ley polarization for either edge plasmon varies monotonously but cannot be perfect.

We study valley-polarized collective motion[31] of electrons in a strained graphene sheet with a boundary $x = 0$. As depicted in the inset of Fig. 10(b), the strain-induced pseudomagnetic field is opposite for electrons in the K and K' valleys, which is assumed to be uniform, i.e., $B_K \equiv B$ and $B_{K'} \equiv -B$. In the Fermi-liquid regime and under the hydrodynamic transport, local electron densities $n_\tau(x,y,t)$ and velocities $\boldsymbol{u}_\tau(x,y,t)$ in the two valleys ($\tau = \pm 1$) satisfy[30,31] the continuity equation, the momentum-balance equation, and the Poisson equation,

$$\frac{\partial n_\tau}{\partial t} + \boldsymbol{\nabla}\cdot(n_\tau \boldsymbol{u}_\tau) = 0, \tag{29}$$

$$\frac{\partial \boldsymbol{u}_\tau}{\partial t} + (\boldsymbol{u}_\tau\cdot\boldsymbol{\nabla})\boldsymbol{u}_\tau = -\frac{e}{m_*}\nabla\phi - \tau\frac{eB}{m_* c}\boldsymbol{e}_z\times\boldsymbol{u}_\tau - \frac{v_{\rm F}^2}{2n_\tau}\nabla n_\tau, \tag{30}$$

$$\nabla^2\phi = 4\pi e(n_{+1} + n_{-1} - 2n_0). \tag{31}$$

Here, Gaussian units are adopted, $m_* = \hbar\sqrt{2\pi n_0}/v_{\rm F}$ is the plasmon mass, n_0 is the initial equilibrium density for both valleys, $v_{\rm F}$ is the Fermi velocity, c is the light velocity, $\boldsymbol{e}_z$ is the normal of the graphene plane, and $\phi(x,y,t)$ is the Coulomb potential due to the electron density fluctuations $n_{\pm1} - n_0$. On the right side of Eq. (30), the three terms are respectively the electrostatic force, the Lorentz force, and the Fermi pressure. Outside the graphene sheet ($x < 0$), both $n_\tau(x,y,t)$ and $\boldsymbol{u}_\tau(x,y,t)$ vanish.

By solving self-consistently these nonlinear two-component hydrodynamic equations, we confirm the existence of valley-polarized edge plasmons caused by strain-induced pseudomagnetic fields in the steady-state limit $t \to +\infty$. In an edge plasmon, both $n_\tau - n_0$ and $\boldsymbol{u}_\tau$ approach zero at positions away from the boundary $x = 0$ (see Fig. 2 of Ref. [31]). As plotted in Fig. 10(a), the electron density $n_{-1}|_{x=0^+}$ in the K' valley exhibits a nonmonotous variation with the pseudomagnetic field B. It reaches the maximum at $B = 17.5$ T and then drops quickly to zero. This drastic change results from the remarkable nonlinear effect in the considered hydrodynamic model. Actually, under a high pseudomagnetic field, the convective velocity term in the momentum-balance equation varies quickly near the edge. The flux corrected transport (FCT) method adopted in the calculation can treat efficiently such a strong nonlinearity. For $B > 19.2$ T, the collective edge plasmon oscillation is only contributed by the density in the K valley. The valley polarization $P_{\rm v}$ of the edge plasmon is defined as the relative difference between n_{+1} and n_{-1} at the boundary

$$P_{\rm v} = \left.\frac{n_{+1}(x,y,t) - n_{-1}(x,y,t)}{n_{+1}(x,y,t) + n_{-1}(x,y,t)}\right|_{x=0^+}. \tag{32}$$

From Fig. 10(b) one can observe that the edge plasmon is firstly K'-polarized for $B \le 17.5$ T, and then becomes K-polarized at $B > 18$ T. A full valley polarization appears at $B = 19.2$ T. The polarity reversal of $P_{\rm v}$ was not observed in the linearized model of Ref. [30]. It is due to the direction change of the longitudinal plasmon velocities under strong pseudomagnetic fields. Under a low pseudomagnetic field, the edge plasmon is always K'-polarized despite the value of initial density n_0. Under a strong pseudomagnetic field, $P_{\rm v}$ can reverse its polarity at a low initial density n_0.

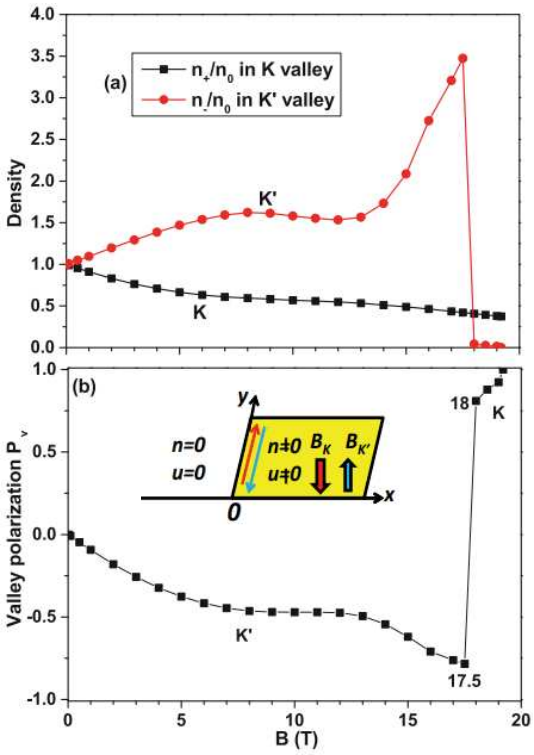


Fig. 10. The variation of (a) normalized density $n_{\pm1}/n_0$ in the K and K' valleys and (b) degree of valley polarization $P_{\rm v}$ at the boundary ($x = 0$ in the inset of panel (b)) with the strength of the pseudomagnetic field B for one edge plasmon mode. For each valley, we take a uniform initial density $n_0 = 6\times10^{10}$ cm^{-2} and set the initial plasmon velocity at the edge at $v_{0\rm i} = 1.2v_{\rm F}$. The valley polarization changes its polarity at $B = 17.5$ T. Reproduced with permission from Ref. [31].

A dynamical control of valley polarization $P_{\rm v}$ is desirable for the applications of valley-polarized edge plasmons. In a graphene mechanical resonator, quantum pumping was proposed to generate valley-polarized bulk currents.[27] For edge pseudomagnetoplasmons in strained graphene, we studied the dynamical control of valley polarization[32] by a time-dependent voltage consisting of multiple harmonics. Without the applied voltage and under a low pseudomagnetic field ($B = 1$ T), there existed two unidirectional-propagating edge-plasmon modes with weak valley polarization $P_{\rm v}$. We demonstrated that both the amplitude and the polarity of $P_{\rm v}$ can be altered by varying the amplitude of multiple harmonics with frequency in the THz regime. Two perfect valley-polarized states, $P_{\rm v} = 1$ and $P_{\rm v} = -1$, can appear successively in a cycle of the multiple harmonics. The frozen valley possesses a

vanishing edge-plasmon density and transverse velocity. With the increasing of time, more electrons away from the edge can contribute to the edge plasmon excitation. During the positive or negative part of the voltage waveform, they move near or further to the edge. Accordingly, the valley polarization under a weak multiple harmonics increases with time and can become significant after several cycles.

5.2. Valley-polarized surface magnetoplasmons

Electron hydrodynamics provides a universal long-wavelength description of collective plasmon modes in many-body systems.[125–128] For an electron system in graphene with an ultrahigh mobility, momentum-conserving electron–electron collisions are the dominant scattering process at low temperatures so that electron transport behaves as a hydrodynamic flow. The hydrodynamic effect of electron fluids in graphene was reported by several groups.[125–127]

For 2D electron systems with broken inversion symmetry and under a vertical magnetic field, a theory of electron hydrodynamics was formulated in Ref. [129]. In the hydrodynamic equations, novel terms emerge due to the coupling of the magnetic field, Berry curvature and OMM, which lead to nonreciprocal surface magnetoplasmons and the nonreciprocity in magneto-optical responses. Here surface magnetoplasmons refer to collective excitations of electrons coupled to the electromagnetic field at an interface between a dielectric material and graphene under a vertical static magnetic field. Nonreciprocal responses are characterized by the directional transport of particles, which enable the one-way chiral mode of the information carrier.[130]

We study the influence of the valley Zeeman effect on electron hydrodynamics[54] in a graphene monolayer with a hexagonal boron nitride (h-BN) film on top. The coupling between h-BN and graphene in Fig. 11(a) brings a sublattice-staggered potential and strain-related vector potential $\boldsymbol{A}_{\rm S}$ for electrons in graphene. The sublattice-staggered potential gives a mass gap, allowing a finite OMM and Berry curvature (see Eqs. (23) and (25)). The system is modulated by a uniform vertical magnetic field B_0 and a transverse magnetic wave propagating with frequency ω, wave vector $\boldsymbol{k}=(k_x,k_y)$, and perpendicular magnetic field $B_{z1}=B_1\exp(-{\rm i}\omega t)$. In the hydrodynamic regime, the electron system in graphene reaches a local equilibrium through electron–electron scatterings, which results in a local equilibrium distribution

$$f_{\rm local}(\boldsymbol{r},\boldsymbol{p},\tau)=\left[{\rm e}^{(E_\tau(\boldsymbol{p})-\boldsymbol{u}_\tau\cdot\boldsymbol{p}-\mu)/(k_{\rm B}T)}+1\right]^{-1}. \tag{33}$$

Here $E_\tau(\boldsymbol{p})=E(\boldsymbol{p})-B_{\rm tot}m_z(\boldsymbol{p})$ is the energy of an electron with quasimomentum $\boldsymbol{p}$ and valley index τ under magnetic field $B_{\rm tot}=B_0+B_{z1}$, $m_z(\boldsymbol{p})$ is the OMM given by Eq. (25), the valley-dependent drift velocity $\boldsymbol{u}_\tau$ may vary with the position $\boldsymbol{r}$ and time t, $k_{\rm B}$ is the Boltzmann constant, T is the temperature, and μ is the chemical potential.

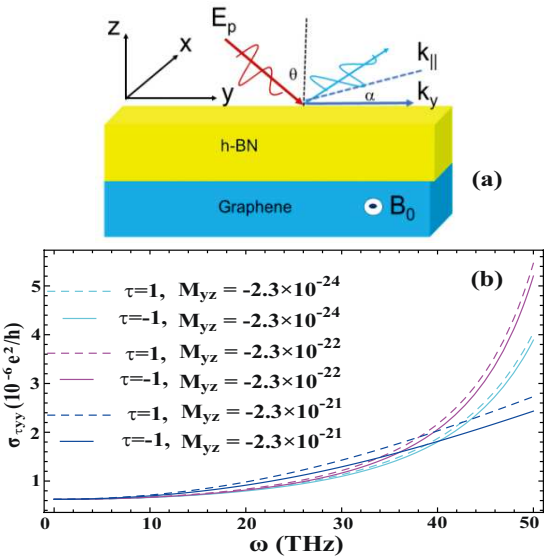


Fig. 11. (a) Schematics of Kretschmann configuration: a hexagonal boron nitride film (h-BN) placed on a graphene monolayer. Electrons in graphene are modulated by a perpendicular magnetic field (B_0) and a transverse magnetic wave with frequency ω. The propagation direction of the incident light is determined by the angles α and θ. (b) Real part of conductivity component $\sigma_{\tau yy}$ in K ($\tau=1$) and K' ($\tau=-1$) valleys at $B_0=3.5$ kG, $\alpha=3\pi/8$ and different values of the geometrical tensor component M_{yz} (in unit of g·cm/s). Reproduced with permission from Ref. [54].

By multiplying the Boltzmann equation with the quasiparticle velocity and then summing over all single-particle states[129,131] with the distribution function (33), one yields the continuity equation and Euler equation for electron density n_τ and drift velocity $\boldsymbol{u}_\tau$. The extremes of OMM and Berry curvature in the momentum space are valley-resolved due to the strain-related vector potential. As a result, in the generalized Euler equation,[129] an anomalous driving force appears, which is proportional to the vertical magnetic field and a geometrical tensor $\boldsymbol{M}$. Indeed, $\boldsymbol{M}$ is the integral over occupied states for the momentum gradient of the OMM, which is peculiar to the noncentrosymmetric fluids. The anomalous driving force due to $\boldsymbol{M}$ is similar to the Stern–Gerlach force for a spinful particle moving in a nonuniform magnetic field.

One can derive the linear optical conductivity tensor[54] $\boldsymbol{\sigma}_{\tau ij}$ for a small deviation of the hydrodynamic velocity from its equilibrium value. Here $i,j\in\{x,y\}$ represents the direction of local current and the electric field of light. For $\boldsymbol{A}_{\rm S}$ along the y direction, the diagonal optical conductivity $\sigma_{\pm yy}$ is shown in Fig. 11(b). Here the geometrical tensor $\boldsymbol{M}$ has only a nonzero component M_{yz}. One can observe a valley splitting for the longitudinal conductivity in all cases. The valley separation increases with the light frequency ω and the amplitude of M_{yz}. We check that this valley splitting disappears when the valley Zeeman effect turns off. The valley separation of optical conductivity can be tuned by the direction (angle α) of the

incident light. The nondiagonal optical conductivity satisfies $\sigma_{-ij} = -\sigma_{+ij}$ and the nonreciprocity $\sigma_{\tau xy} \neq \sigma_{\tau yx}$.

6. Recent progress of valleytronics beyond graphene

Symmetry-breaking fields including mechanical strain, electric and magnetic fields, were also utilized to tune the valley polarization of other 2D materials. By fabricating a strain-inducing grating on the surface of an AlAs quantum well, Mueed *et al.*[132] realized a valley superlattice, i.e., a valley-related spatial modulation of electron population. In newly discovered ferroelectric SnTe monolayers, standing waves of holes confined by electrically neutral domain walls were observed.[133] This novel confinement was ascribed to the partial lift of valley degeneracy under the ferroelectric phase transition and the momentum mismatch of holes across neighboring domains. In piezotronic valley transistors made of normal/ferromagnetic/normal structure of monolayer TMDs, Rabi frequency approaching 4200 MHz was reported.[134] The strain-induced strong polarization can be applied to manipulate the valley qubit. In conventional valleytronic materials, it is usually difficult to generate valley polarization only by a gate field. The inspiring concept of valley-layer coupling[135] in some 2D materials (such as monolayer TiSiCO) harnessed electronic states with valley-contrasted layer polarization. It provides an all-electric means to tune continuously the polarity and amplitude of the valley polarization.

It was reported theoretically that[136] in $VAgP_2Se_6$ monolayer with suitable doping, the Zeeman-type valley splitting results in a permanent valley polarization, which can be used to design a valley pseudospin field effect transistor. Valley-mechanical interaction[137] was realized in a resonator made of monolayer MoS_2 by the application of a magnetic field gradient. As the valleys were populated optically, mechanical actuation was observed by means of laser interferometry. Accordingly, valley information was transduced into mechanical states. In a twisted bilayer graphene under perpendicular magnetic fields, Berdyugin *et al.*[138] reported selective focusing of electrons in different minivalleys by voltage bias between the layers. It was predicted that[139] intrinsic ferromagnetic 2H-$RuCl_2$ and Janus VSSe monolayers host nontrivial corner states along different magnetization directions and huge valley polarization. These materials could provide platform for valleytronics and topological spintronics.

The effect of electron–electron and electron–phonon interaction on valley polarization was examined recently. In an itinerant electron system, Hossain *et al.*[140] demonstrated theoretically that the electron–electron interaction prefers single-valley occupancy of electrons below a critical density. Consequently, one can switch the valley polarization from 0 to 1 by a small reduction in density and thus design a valleytronic transistor device. In TMDs under circularly polarized light, phonon-limited valley polarization was calculated by Lin *et al.*[141] entirely from the first principles, which is around 70% at room temperature. In both n- and p-type valleytronic transistors made of monolayer MoS_2 and WSe_2, a large valley on–off ratio (nearly 10^4) was reported experimentally.[142]

7. Conclusions and outlook

We have provided an overview of valley filtering and valley-polarized collective modes in bulk graphene monolayers. The valley-related interactions concerned include the strain-induced pseudomagnetic fields and associated vector potential, the gap due to the sublattice-stagger potential, and the valley-Zeeman effect. Theoretical investigations have demonstrated the features and mechanism of valley filtering in bulk graphene monolayers due to these valley-related interactions and local magnetic fields or magnetic proximity. On the other hand, these valley-related interactions can be utilized to obtain valley spatial separation, valley-resolved guiding modes, and valley-polarized edge or surface plasmons.

Although great triumphs have been achieved in graphene valleytronics, there are still some fundamental theoretical questions to be solved. A basic problem in valleytronics is to define a proper physical quantity to characterize the valley-polarized current and pure valley current. In spintronics, how to define properly a spin current in spin-nonconserved systems is of controversy.[143] The valley current is actually fictitious due to the absence of an associated physical operator. The valley index of a propagating state is usually determined by the distance between its momentum to the valley points. This description needs an artificial cutoff for the valley-restricted integrals in the valley Hall conductivity. For gapped graphene where the valley Hall effect was observed, Bhowal and Vignale[144] argued that the ambiguous valley indices can be replaced by the OMM. Accordingly, the valley Hall effect belongs to the orbital Hall effect and can be described by the physical quantity called valley orbital Hall conductivity. However, this approach cannot be applied to the gapless case and depends on special gap terms in the Hamiltonian.

For valley-related transport, intervalley scattering was studied in deformed graphene with merging Dirac cones[145] and in superlattice made of monolayer TMDs.[146] In this case, it is also necessary to find a physical quantity to describe the valley polarization for the output current. The control of intervalley scattering is indispensable for realistic valleytronic applications, which is a challenge for experiments but scarcely studied. For the valley-polarized collective modes in graphene, intervalley scattering leads to propagation loss of plasmon in a specific valley, especially in the presence of strong nonlinear effect.

The proximity effect brings a new perspective to the spintronic applications of graphene. Similarly, the hybridation between graphene and other materials with peculiar crystal or band structures could pave a way for graphene valleytronics. When the substrate has a honeycomb lattice commensurating with graphene, its superlattice potential can be viewed as a pseudomagnetic field that rotates the valley pseudospin.[147,148] Beenakker *et al.*[149] mapped the scattering problem at a pristine-graphene–superlattice–graphene interface onto that of Andreev reflection from a topological superconductor. They predicted that electrons near normal incidence are reflected in the opposite valley. For a sheet of graphene coupled to a Weyl semimetal with appropriate alignment, Khalifa *et al.*[150] demonstrated numerically that the Weyl semimetal can draw away current only in a specific valley of the bulk graphene monolayer. With the rapid development of 2D materials, more valley-related transport phenomena are awaiting to be discovered in graphene-related heterostructure[151] devices.

Acknowledgments

We express our sincere appreciation to our collaborators for their invaluable contributions to the related works presented in this review. This work is supported by the National Natural Science Foundation of China (Grant Nos. 11774314 and 12274370) and Scientific Research Start-up Fund of Zhejiang Normal University (Grant No. YS304222903).

References

[1] Sham L J, Allen S J, Kamgar J A and Tsui D C 1978 *Phys. Rev. Lett.* **40** 472
[2] Ohkawa F J and Uemura Y 1977 *J. Phys. Soc. Jpn.* **43** 907
[3] Gunawan O, Shkolnikov Y P, Vakili K, Gokmen T, De Poortere E P and Shayegan M 2006 *Phys. Rev. Lett.* **97** 186404
[4] Schaibley J R, Yu H Y, Clark G, Rivera P, Ross J S, Seyler K L, Yao W and Xu X D 2016 *Nat. Rev. Mater.* **1** 16055
[5] Vitale S A, Nezich D, Varghese J O, Kim P, Gedik N, Jarillo-Herrero P, Xiao D and Rothschild M 2018 *Small* **14** 1801483
[6] Zhang Y, Jia L G, Chen Y Y, He L and Wang Y L 2022 *Chin. Phys. B* **31** 087301
[7] Tian H Y, Ren C D and Wang S K 2022 *Chin. Phys. B* **33** 212001
[8] Beenakker C W J 2008 *Rev. Mod. Phys.* **80** 1337
[9] Castro Neto A H, Guinea F, Peres N M R, Novoselov K S and Geim A K 2009 *Rev. Mod. Phys.* **81** 109
[10] Rycerz A, Tworzydło J and Beenakker C W J 2007 *Nat. Phys.* **3** 172
[11] Garcia-Pomar J L, Cortijo A and Nieto-Vesperinas M 2008 *Phys. Rev. Lett.* **100** 236801
[12] Deng F S, Sun Y, Wang X, Xue R, Li Y, Jiang H T, Shi Y L, Chang K and Chen H 2014 *Opt. Express* **22** 23605
[13] Gunlycke D and White C T 2011 *Phys. Rev. Lett.* **106** 136806
[14] Kundu A, Fertig H A and Seradjeh B 2016 *Phys. Rev. Lett.* **116** 016802
[15] Yang Q and Tong Q J 2022 *Phys. Rev. B* **106** 115406
[16] Sharma S, Elliott P and Shallcross S 2023 *Sci. Adv.* **9** eadf3673
[17] Zhai F, Zhao X F, Chang K and Xu H Q 2010 *Phys. Rev. B* **82** 115442
[18] Zhai F, Ma Y L and Zhang Y T 2011 *J. Phys.: Condens. Matter* **23** 385302
[19] Song Y, Zhai F and Guo Y 2013 *Appl. Phys. Lett.* **103** 183111
[20] Guinea F, Katsnelson M I and Geim A K 2010 *Nat. Phys.* **6** 30
[21] Low T and Guinea F 2010 *Nano Lett.* **10** 3551
[22] Myoung N, Choi H and Park H C 2020 *Carbon* **157** 578
[23] Li S Y, Su Y, Ren Y N and He L 2020 *Phys. Rev. Lett.* **124** 106802
[24] Ren Y N, Zhuang Y C, Sun Q F and He L 2022 *Phys. Rev. Lett.* **129** 076802
[25] Zhai F, Ma Y L and Chang K 2011 *New J. Phys.* **13** 083029
[26] Wu Z H, Zhai F, Peeters F M, Xu H Q and Chang K 2011 *Phys. Rev. Lett.* **106** 176802
[27] Jiang Y J, Low T, Chang K, Katsnelson M I and Guinea F 2013 *Phys. Rev. Lett.* **110** 046601
[28] Wang J, Chan K S and Lin Z J 2014 *Appl. Phys. Lett.* **104** 013105
[29] Linnik T L 2014 *Phys. Rev. B* **90** 075406
[30] Principi A, Katsnelson M I and Vignale G 2016 *Phys. Rev. Lett.* **117** 196803
[31] Zhang Y, Guo B, Zhai F and Jiang W 2018 *Phys. Rev. B* **97** 115455
[32] Zhang Y, Guo B, Zhai F and Jiang W 2018 *Opt. Express* **26** 33453
[33] Zhang X P, Huang C L and Cazalilla M A 2017 *2D Mater.* **4** 024007
[34] Yu H, Kutana A and Yakobson B 2022 *Nano Lett.* **22** 2934
[35] Prabhakar S, Nepal R, Melnik R and Kovalev A A 2019 *Phys. Rev. B* **99** 094111
[36] Ortiz W, Szpak N and Stegmann T 2020 *Phys. Rev. B* **106** 035416
[37] Jung M, Fan Z Y and Shvets G 2018 *Phys. Rev. Lett.* **121** 086807
[38] An X T, Xiao J, Tu M W Y, Yu H Y and Yao W 2017 *Phys. Rev. Lett.* **118** 096602
[39] An X T and Yao W 2020 *Phys. Rev. Appl.* **14** 014039
[40] Tu M W Y and Yao W 2017 *2D Mater.* **4** 025109
[41] Xiao D, Yao W and Niu Q 2007 *Phys. Rev. Lett.* **99** 236809
[42] Martin I, Blanter Y M and Morpurgo A F 2008 *Phys. Rev. Lett.* **100** 036804
[43] Semenoff G W, Semenoff V and Zhou F 2008 *Phys. Rev. Lett.* **101** 087204
[44] Yao W, Yang S A and Niu Q 2009 *Phys. Rev. Lett.* **102** 096801
[45] Li J, Wang K, McFaul K J, Zern Z, Ren Y, Watanabe K, Taniguchi T, Qiao Z and Zhu J 2016 *Nat. Nanotechnol.* **11** 1060
[46] Chen H, Zhou P, Liu J, Qiao J, Oezyilmaz B and Martin J 2020 *Nat. Commun.* **11** 1202
[47] Li J, Zhang R X, Yin Z X, Zhang J X, Watanabe K, Taniguchi T, Liu C X and Zhu J 2018 *Science* **362** 1149
[48] Wang Z B, Cheng S G, Liu X and Jiang H 2021 *Nanotechnology* **32** 402001
[49] Zhai F and Chang K 2012 *Phys. Rev. B* **85** 155415
[50] Zhai F 2012 *Nanoscale* **4** 206527
[51] Moldovan D, Masir M R, Covaci L and Peeters F M 2012 *Phys. Rev. B* **86** 115431
[52] Lins A R S and Lima J R F 2020 *Carbon* **157** 578
[53] Grujic M M, Tadic M Z and Peeters F M 2014 *Phys. Rev. Lett.* **113** 046601
[54] Zhang Y, Zhai F and Jiang W 2023 *Appl. Surf. Sci.* **619** 156717
[55] Wang J and Fischer S 2014 *Phys. Rev. B* **89** 245421
[56] Gmitra M and Fabian J 2015 *Phys. Rev. B* **92** 155403
[57] Alsharari A M, Asmar M M and Ulloa S E 2016 *Phys. Rev. B* **94** 241106
[58] Cummings A W, Garcia J H, Fabian J and Roche S 2017 *Phys. Rev. Lett.* **119** 206601
[59] Gmitra M and Fabian J 2017 *Phys. Rev. Lett.* **119** 146401
[60] Dyrdal A and Barnas J 2017 *2D Mater.* **4** 034003
[61] Bora M, Behera S K, Samal P and Deb P 2022 *Phys. Rev. B* **105** 235422
[62] Zheng J L, Lu J Q and Zhai F 2022 *Phys. Rev. B* **105** 165410
[63] Forsythe C, Zhou X D, Watanabe K, Taniguchi T, Pasupathy A, Moon P, Koshino M, Kim P and Dean C R 2018 *Nat. Nanotechnol.* **13** 566
[64] Martiny J H J, Kaasbjerg K and Jauho A P 2019 *Phys. Rev. B* **100** 155414
[65] Aktor T, Garcia J H, Roche S, Jauho A P and Power S R 2021 *Phys. Rev. B* **103** 115406
[66] Zutic I, Fabian J and Sarma S D 2004 *Rev. Mod. Phys.* **76** 323
[67] Zhou S Y, Gweon G H, Fedorov A V, First P N, de Heer W A, Lee D H, Guinea F, Castro Neto A H and Lanzara A 2007 *Nat. Mater.* **6** 770
[68] Kim S, Ihm J, Choi H J and Son Y W 2008 *Phys. Rev. Lett.* **100** 176802
[69] Vitali L, Riedl C, Ohmann R, Brihuega I, Starke U and Kern K 2008 *Surf. Sci.* **602** 127
[70] Li G H, Luican A and Andrei E Y 2009 *Phys. Rev. Lett.* **102** 176804
[71] Enderlein C, Kim Y S, Bostwick A, Rotenberg E and Horn K 2010 *New J. Phys.* **12** 033014
[72] Cuong N T, Otani M and Okada S 2011 *Phys. Rev. Lett.* **106** 106801
[73] Zanella I, Guerini S, Fagan S B, Mendes F J and Souza F A G 2008 *Phys. Rev. B* **77** 073404

[74] Ribeiro R M, Peres N M R, Coutinho J and Briddon P R 2008 *Phys. Rev. B* **78** 075442
[75] Zhai F and Xu H Q 2005 *Phys. Rev. Lett.* **94** 246601
[76] Kubrak V, Rahman F, Gallagher B L, Main P C, Henini H, Marrows C H and Howson M A 1999 *Appl. Phys. Lett.* **74** 2507
[77] Nogaret A, Bending S J and Henini M 2000 *Phys. Rev. Lett.* **84** 2231
[78] Vančura T, Ihn T, Broderick S, Ensslin K, Wegscheider W and Bichler M 2000 *Phys. Rev. B* **62** 5074
[79] Nogaret A, Lawton D N, Maude D K, Portal J C and Henini M 2003 *Phys. Rev. B* **67** 165317
[80] Hong J, Joo S, Kim T S, Rhie K, Kim K H, Kim S U, Lee B C and Shin K H 2007 *Appl. Phys. Lett.* **90** 023510
[81] Tarasov A, Hugger S, Xu H Y, Cerchez M, Heinzel T, Zozoulenko I V, Gasser-Szerer U, Reuter D and Wieck A D 2010 *Phys. Rev. Lett.* **104** 186801
[82] Johnson M, Bennett B R, Yang M J, Miller M M and Shanabrook B V 1997 *Appl. Phys. Lett.* **71** 974
[83] Lee S J, Souma S, Ihm G and Chang K J 2004 *Phys. Rep.* **394** 1
[84] Xu H Q 1994 *Phys. Rev. B* **50** 8469
[85] Zhai F and Lu J Q 2016 *Phys. Rev. B* **94** 165426
[86] Pereira V M and Castro Neto A H 2009 *Phys. Rev. Lett.* **103** 046801
[87] Ni Z H, Yu T, Lu Y H, Wang Y Y, Feng Y P and Shen Z X 2008 *ACS Nano* **2** 2301
[88] Huang M Y, Yan H G, Chen C Y and Hone J 2009 *Proc. Natl. Acad. Sci. USA* **106** 7304
[89] Zheng J L, Lu J Q and Zhai F 2021 *Nanotechnology* **32** 025205
[90] Zhou X F, Dong X, Oganov A R, Zhu Q, Tian Y and Wang H T 2014 *Phys. Rev. Lett.* **112** 085502
[91] Koga T, Nitta J, Takayanagi H and Datta S 2002 *Phys. Rev. Lett.* **88** 126601
[92] Khodas M, Shekhter A and Finkel'stein A M 2004 *Phys. Rev. Lett.* **92** 086602
[93] Cheianov V V, Fal'ko V and Altshuler B L 2007 *Science* **315** 1252
[94] Moghaddam A G and Zareyan M 2010 *Phys. Rev. Lett.* **105** 146803
[95] Goos F and Hänchen H 1947 *Ann. Phys.* **436** 333
[96] Beenakker C W J, Sepkhanov R A, Akhmerov A R and Tworzydlo J 2009 *Phys. Rev. Lett.* **102** 146804
[97] Young A F and Kim P 2009 *Nat. Phys.* **5** 222
[98] Park C H, Son Y W, Yang L, Cohen M L and Louie S G 2008 *Nano Lett.* **8** 2920
[99] Williams J R, Low T, Lundstrom M S and Marcus C M 2011 *Nat. Nanotechnol.* **6** 222
[100] Li C F 2003 *Phys. Rev. Lett.* **91** 133903
[101] Zhou X X, Zheng J L and Zhai F 2022 *Commun. Theor. Phys.* **74** 075701
[102] Saitoh E, Ueda M, Miyajima H and Tatara G 2006 *Appl. Phys. Lett.* **88** 182509
[103] Valenzuela S O and Tinkham M 2006 *Nature* **442** 176
[104] Recher P, Nilsson J, Burkard G and Trauzettel B 2009 *Phys. Rev. B* **79** 085407
[105] Gorbachev R V, Song J C W, Yu G L, Kretinin A V, Withers F, Cao Y, Mishchenko A, Grigorieva I V, Novoselov K S, Levitov L S and Geim A K 2014 *Science* **346** 448
[106] Shimazaki Y, Yamamoto M, Borzenets I V, Watanabe K, Taniguchi T and Tarucha S 2015 *Nat. Phys.* **11** 1032
[107] Lee Y, Knothe A, Overweg H, Eich M, Gold C, Kurzmann A, Klasovika V, Taniguchi T, Wantanabe K, Fal'ko V, Ihn T, Ensslin K and Rickhaus P 2020 *Phys. Rev. Lett.* **124** 126802
[108] Ge Z H, Slizovskiy S, Joucken F, Quezada E A, Taniguchi T, Watanabe K, Fal'ko V I and Velasco J 2021 *Phys. Rev. Lett.* **127** 136402
[109] Park C 2019 *Phys. Rev. Appl.* **11** 044033
[110] Park C 2018 *Phys. Lett. A* **382** 121
[111] Yang H X, Hallal A, Terrade D, Waintal X, Roche S and Chshiev M 2013 *Phys. Rev. Lett.* **110** 046603
[112] Wang Z Y, Tang C, Sachs R, Barlas Y and Shi J 2015 *Phys. Rev. Lett.* **114** 016603
[113] Leutenantsmeyer J C, Kaverzin A A, Wojtaszek M and Van Wees B J 2017 *2D Mater.* **4** 014001
[114] Wei P, Lee S, Lemaitre F, Pinel L, Cutaia D, Cha W, Katmis F, Zhu Y, Heiman D, Hone J, Moodera J S and Chen C T 2016 *Nat. Mater.* **15** 711
[115] Klein D R, MacNeill D, Lado J L, Soriano D, Navarro-Moratalla E, Watanabe K, Taniguchi T, Manni S, Canfield P, Fernández-Rossier J and Jarillo-Herrero P 2018 *Science* **360** 1218
[116] Song Y 2018 *J. Phys. D: Appl. Phys.* **51** 025002
[117] Solis D A, Hallal A, Waintal X and Chshiev M 2019 *Phys. Rev. B* **100** 104402
[118] Evelt M, Ochoa H, Dzyapko O, Demidov V E, Yurgens A, Sun J, Tserkovnyak Y, Bessonov V, Rinkevich A B and Demokritov S O 2017 *Phys. Rev. B* **95** 024408
[119] Hallal A, Ibrahim F, Yang H, Roche S and Chshiev M 2017 *2D Mater.* **4** 025074
[120] Mast D B, Dahm A J and Fetter A L 1985 *Phys. Rev. Lett.* **54** 1706
[121] Kumada N, Roulleau P, Roche B, Hashisaka M, Hibino H, Petković I and Glattli D C 2014 *Phys. Rev. Lett.* **113** 266601
[122] Jin D F, Lu L, Wang Z, Fang C, Joannopoulos J D, Soljačić M, Fu L and Fang N X 2016 *Nat. Commun.* **7** 13486
[123] Levy N, Burke S A, Meaker K L, Panlasigui M, Zettl A, Guinea F, Castro Neto A H and Crommie M F 2010 *Science* **544** 13486
[124] Hsu C C, Teague M L, Wang J Q and Yeh N C 2020 *Sci. Adv.* **6** eaat9488
[125] Bandurin D A, Torre I, Kumar R K, Ben S M, Tomadin A, Principi A, Auton G H, Khestanova E, Novoselov K S, Grigorieva I V, Ponomarenko L A, Geim A K and Polini M 2016 *Science* **351** 1055
[126] Crossno J, Shi J K, Wang K, Liu X, Harzheim A, Lucas A, Sachdev S, Kim P, Taniguchi T, Watanabe K, Ohki T A and Fong K C 2016 *Science* **351** 1058
[127] Berdyugin A I, Xu S G, Pellegrino F M D, Krishna K R, Principi A, Torre I, Ben Shalom M, Taniguchi T, Watanabe K, Grigorieva I V, Polini M, Geim A K and Bandurin D A 2019 *Science* **364** 162
[128] Vool U, Hamo A, Varnavides G, Wang Y, Zhou T X, Kumar N, Dovzhenko Y, Qiu Z, Garcia C A C, Pierce A T, Gooth J, Anikeeva P, Felser C, Narang P and Yacoby A 2021 *Nat. Phys.* **17** 1216
[129] Sano R, Toshio R and Kawakami N 2021 *Phys. Rev. B* **104** L241106
[130] Tokura Y and Nagaosa N 2018 *Nat. Commun.* **9** 3740
[131] Lucas A and Fong K C 2018 *J. Phys.: Condens. Matter* **30** 053001
[132] Mueed M A, Hossain M S, Jo I, Pfeiffer L N, West K W, Baldwin K W and Shayegan M 2018 *Phys. Rev. Lett.* **121** 036802
[133] Chang K, Miller B J, Yang H, Lin H C, Parkin S S P, Barraza-Lopez S, Xue Q K, Chen X and Ji S H 2019 *Phys. Rev. Lett.* **122** 206402
[134] Liu R H, Zhang Y M, Zhou Y K, Nie J H, Li L J and Zhang Y 2023 *Nano Energy* **113** 108550
[135] Yu Z M, Guan S, Sheng X L, Gao W B and Yang S A 2020 *Phys. Rev. Lett.* **124** 037701
[136] Song Z G, Sun X T, Zheng J X, Pan F, Hou Y L, Yung M H, Yang J B and Lu J 2018 *Nanoscale* **10** 13986
[137] Li H K, Fong K Y, Zhu H Y, Li Q W, Wang S Q, Yang S, Wang Y and Zhang X 2019 *Nat. Photonics* **13** 397
[138] Berdyugin A I, Tsim B, Kumaravadivel P, Xu S G, Ceferino A, Knothe A, Kumar R K, Taniguchi T, Watanabe K, Geim A K, Grigorieva I V and Fal'ko V I 2020 *Sci. Adv.* **6** 7838
[139] Li R H, Mao N, Wu X M, Huang B B, Dai Y and Niu C W 2023 *Nano Lett.* **23** 91
[140] Hossain M S, Ma M K, Villegas-Rosales K A, Chung Y J, Pfeiffer L N, West K W, Baldwin K W and Shayegan M 2021 *Phys. Rev. Lett.* **127** 116601
[141] Lin Z Z, Liu Y Z, Wang Z, Xu S N, Chen S Y, Duan W H and Monserrat B 2022 *Phys. Rev. Lett.* **129** 027401
[142] Lai S, Zhang Z W, Wang N Z, Rasmita A, Deng Y, Liu Z and Gao W B 2023 *Nano Lett.* **23** 192
[143] Shi J R, Zhang P, Xiao D and Niu Q 2006 *Phys. Rev. Lett.* **96** 076604
[144] Bhowal S and Vignale G 2021 *Phys. Rev. B* **103** 195309
[145] Ang Y S, Yang S Y A, Zhang C, Ma Z S and Ang L K 2017 *Phys. Rev. B* **96** 245410
[146] Mu H Y, Yao Y T, Li J R, Liu G C, He C, Sun Y J, Yang G, An X T, Zhang Y Z and Liu J J 2020 *J. Phys. Chem. Lett.* **11** 3882
[147] Giovannetti G, Capone M, van den Brink J and Ortix C 2015 *Phys. Rev. B* **91** 121417(R)
[148] Venderbos J W F, Manzardo M, Efremov D V, van den Brink J and Ortix C 2016 *Phys. Rev. B* **93** 045428
[149] Beenakker C W J, Gnezdilov N V, Dresselhaus E, Ostroukh V P, Herasymenko Y, Adagideli I and Tworzydlo J 2018 *Phys. Rev. B* **97** 241403(R)
[150] Khalifa A M, Kaul R K, Shimshoni E, Fertig H A and Murthy G 2021 *Phys. Rev. Lett.* **127** 126801
[151] Pham P V, Bodepudi S C, Shehzad K, Liu Y, Xu Y, Yu B and Duan X F 2022 *Chem. Rev.* **122** 6514